Electrical Conductivities Studies of Nano-Zero-Valent Iron and Their Silica-Based Composites at Different Temperatures

I. S. El-Hallag*[1], A. A. Al-Owais[2] and E. H. El-Mossalamy[3]

[1]*Chemistry Department, Faculty of Science, Tanta University, Tanta, Egypt*
[2]*Chemistry Department, College of Science, King Saud University, Saudi Arabia*
[3]*Chemistry Department, Faculty of Science, Benha University, Benha, Egypt*
*Corresponding author: i.elhallag@yahoo.com

Received 07/01/2025; accepted 28/04/2025
https://doi.org/10.4152/pea.2027450205

Abstract
Nanoscale zero-valent iron (nZVI) is considered the most effective remediation material for contaminated soils, especially by heavy metals. In this case, nZVI were extracted from two different iron salt precursors, $FeCl_3$ (FC) and $Fe(NO_3)_3$ (FN), and then coated onto SiO_2, at 650 and 800 ºC. Synthesis of nZVI was carried out in a C_2H_6O medium, under N atmospheric conditions, using $Fe3^+$ with $Fe(NO_3)_3$ and $FeCl_3$, as counter ions, and $NaBH_4$ as reducing agent. XRD and SEM were used to characterize structures of nZVI. Furthermore, electrical properties of nZVI produced in an aqueous medium were examined.

***Keywords*:** electrical conductivity; FC; FN; nZVI; SiO_2.

Introduction•

Nanoscale materials have received a lot of attention lately, due to their unique properties that distinguish them from bulk materials. Interestingly, there may be scientific and technological uses for zerovalent metal nanostructures, such as as Fe [1, 2], Co [3, 4], Ni [3] or their equivalent composites. Biomedicine [4], environmental remediation [1, 5], energy storage and harvesting [6], and catalysis [3] are only a few of the fields where metallic nanostructures are promising prospects, due to their exceptional physical characteristics. For uses in computer technology, bio imaging, electronics, optics, photonics, data storage and high-frequency applications, it is essential to research magnetic and dielectric characteristics of nanomaterials. Final materials' structure and dielectric and magnetic characteristics are significantly influenced by conditions and methods employed during synthesis. In the studies by [7, 8], several cobalt ferrite nanoparticles by hydrothermal preparation have been produced at different reaction

• The abbreviations and symbol definition lists are in page 144.

temperatures. The authors have found that the sample produced at the highest temperature had the highest saturation magnetization (150.67 emu/g). Nevertheless, synthesis temperature has no effect on dielectric properties.

Nanoscale metallic particles can be obtained in two basic ways: "top-down" and "bottom-up." Grinding of bulk metals serves as an example of how top-down approaches are hindered by narrow particle size distributions [9]. On the other hand, bottom-up methods produce an appropriate constrained range of particle sizes. This method starts with atomic or molecular precursors in gas or solution phases, which accumulate nuclei. These nuclei then gradually develop until they form a nanoparticle. Kinetic characteristics, such as temperature, concentrations and types of stabilizing agents, cause nanoparticles to take on various sizes, shapes and configurations. In recent decades, bottom-up techniques such as chemical reduction, hydrogenation [9] or precipitation [10] have been used to create manufactured nanoparticles for zero-valent iron. For environmental reasons, reduction of Fe(II) or Fe(III) cation solutions using borohydride anion, as depicted by reaction in Eq. (1), is the most popular technique [11].

$$2FeCl_3 + 6NaBH_4 + 18H_2O \rightarrow 2Fe^0 + 6NaCl + 6B(OH)_3 + 21H_2 \qquad (1)$$

Several aqueous media types are crucial for maintaining iron in its zerovalent forms, which constitutes the majority of ore. Mixed oxides such as Fe_3O_4, Fe_2O_3 and FeOOH make up the shell of nanoscale zero-valent (nZVI) iron particle, which often has a core-shell structure [12]. Due to its effective electron donation, this type of metallic iron forms a mixed oxide/hydroxide shell that influences nZVI's bulk composition, surface charge and morphologies. Consequently, surface oxidation, aggregation propensity, magnetic characteristics and environmental interactions are affected.

Iron can react with oxygen carriers in a variety of ways, oxidizing to produce a sub-oxide shell. It is expected that this oxidation reaction generates a very high rate of heat, particularly for ultra-small particles [13]. Many studies have been conducted on oxidation of bulk iron by oxygen and water vapor [14, 15], and of metallic nanoparticles and metal films, at low temperatures, when exposed to oxygen gas [16].

Oxidation of iron nanoparticles occurs in three stages: Fe_3O_4 partially oxidizes into α-Fe_2O_3 structure; Fe_3O_4 and iron core fully oxidize into α-Fe_2O_3 phase; and Fe core oxidizes into crystalline iron oxides and disordered phase formation [17]. Additionally, research shows that the amount of heat reaction may vary depending on size, shape and geometries of iron nanoparticles. High-temperature oxidation processes involving different nanoscale particle sizes should be carefully understood. It has been established that the successful use of nZVI in water purification is due to its increased stability and sustained reactivity [18, 19]. Synthesis of nZVI in aqueous circumstances has been the subject of numerous research articles in recent years.

However, formation of iron nanoparticles in C_2H_6O has not been sufficiently studied. Therefore, the goal of the present study was to synthesize nZVI outdoors using C_2H_6O, while also defining size and surface properties of the materials, in order to prevent severe oxidation [11]. Herein, iron-based nanoparticles in zero-oxidation condition have been synthesized and investigated. Materials were characterized using XRD, SEM, electrical conductivity, real and imaginary components of the dielectric constant, and loss tangent (tan δ) approaches. Overall, the aim of these studies was to gain a thorough understanding of how temperature affects nZVI-SiO_2 composites' electrical characteristics, stability, reactivity and overall performance. Findings can assist to ensure that these materials function well at a wide range of temperatures, maximizing their use in several applications, such as environmental remediation, electrochemical energy systems, catalysis and sensors.

Experimental

Materials

$FeCl_3$ (FC), $NaBH_4$ and $Fe(NO_3)_3$ (FN) were obtained from Sigma-Aldrich Chemical Company. These materials were all used without any further refining. Commercial Na_2SiO_3 solution with a solid concentration of 45% was employed, as well as Al foils and scraps, and plates containing 98% NaOH. Deionized water was used, and all other reagents were analytical grade.

Method

This work focused on the production of nZVI from different counter-ions impregnated with SiO_2. In a flask reactor of three open necks filled up with an C_2H_6O medium, iron nanoparticles were created by reduction using $NaBH_4$, as shown in Fig. 1. Reaction was as follows:

$$2FeX_n + 6NaBH_4 + 18H_2O \rightarrow 2Fe^0 + 6NaX + 6B(OH)_3 + 21H_2 \qquad (2)$$

where X = Cl^- and NO_3^-.

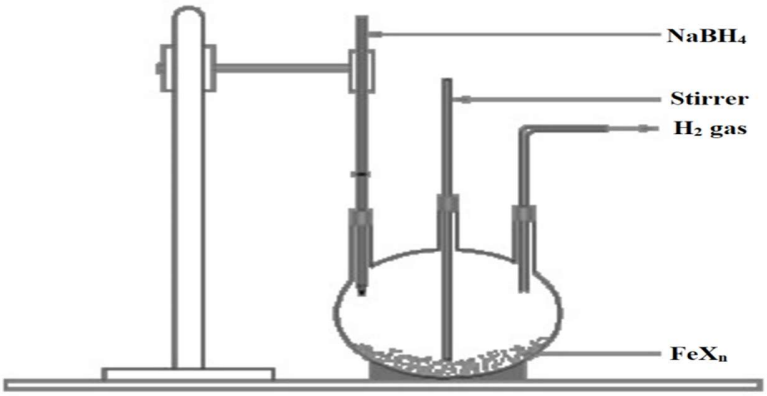

Figure 1: Schematic diagram for synthesis of iron and its composite nanoparticles.

Preparation of nZVI particles

In order to prepare nZVI employing $NO_3^-$and Cl^- anions, a solution of 0.6 M each from Fe0/Cl^- (A) and Fe0/NO_3^-salts (B) was dissolved in a 4/L (v/v) mixture made of 24 mL C_2H_6O + 6 mL deionized water, and thoroughly stirred. Afterwards, to prepare a 0.8 mol L^{-1} $NaBH_4$ solution, 3.028 g of this compound were dissolved in 100 mL deionized water, since more borohydride was needed to boost the creation of iron nanoparticles.

The $NaBH_4$ solution was poured into a burette and forcefully agitated when each solution was added drop by drop, one drop every two secs. When the first drop of $NaBH_4$ solution was added, black solid particles immediately appeared. Remaining $NaBH_4$ was then gradually added to accelerate reduction reaction. After adding whole $NaBH_4$ solution, the mixture was agitated for 30 min. Using vacuum filtration method, liquid phase was isolated from black iron nanoparticles. Using 25 mL portions of 100% C_2H_6O, solid particles were carefully cleaned thrice to remove all water. Perhaps the most important stage in the production process was washing, which stops zero-valent iron nanoparticles from oxidizing too quickly. Finally, resulting nanoparticles were dried at 60 ºC, for a full night. Before being stored, a thin coating of C_2H_6O was added to prevent nano iron particles from oxidizing.

Preparation of SiO_2 nanoparticles

In order to produce SiO_2 nanoparticles, nitric acids and fuels (fructose and glucose) were employed as oxidant and reductant precursors, respectively, using a sol-gel auto-combustion technique. Samples of SiO_2 generated with glucose and fructose were designated S_g and S_f, respectively. For combustion, stoichiometric compositions of redox mixtures were determined by total oxidizing and reducing valences of fuel and oxidizer, to ensure that equivalency ratio, ϕ_c, was unity (i.e., ϕc 1), which maximized energy released during combustion for every process [20].

A typical synthesis process was used to dissolve 6 g SiO_2 gel by whirling it in a hot 50 mL of a 4 mol/L^{-1} $NaBH_4$ solution. Then, a colorless gel was produced by adding 50 mL of 4 M HNO_3 dropwise to the prepared solution. By vigorously washing the produced gel several times with diluted HNO_3, excess NaOH was removed. The mixture's pH was adjusted to 8 with 0.1 mol/L^{-1} HNO_3. Afterwards, the solution was heated to 80 °C, and stirred for 1 h, using a 20 mL aqueous hot solution that contained 3.963 g/0.02 mol glucose or 3.603 g/0.02 mol/L^{-1} fructose. The mixture gelled when it reached 120 °C. Once the gel was formed, a dry gray mass was produced by burning it at 350 °C on a hot plate. Samples S_g and S_f were then created by calcining this bulk, for 4 h, at 800 °C, in an electric furnace.

Impregnation of nZVI with SiO_2

SiO_2 was the carrier for nZVI. Two stages were required to create nZVI utilizing SiO_2: Fe^0/NO_3^-impregnated with Sf (F) and with Sg (E). First, SiO_2 was adsorbed or

wet-impregnated with ferric salts, such as FC or FN. NaBH4 was then used to convert loaded iron to Fe^0 [21]. In the adsorption procedure, 2 g SiO_2 were combined with 20 mL of a 1 mol/L FC or FN solution. The mixture was shaken for 24 h, using a rotary shaker that was set at 25 ºC. Following that, 15 mL each of C_2H_6O and water were added to the mixture. 50 mL of 1 mol/L^{-1} $NaBH_4$ was then added to the mixture, while the liquid was being dropped and vigorously swirled. The final step involved drying generated nanoparticles in an oven set to 60 ºC, for the whole night.

Powder X-ray diffractometer

Generated products were assessed for phase purity and crystallinity by powder XRD, using a Bruker 18 KW diffractometer (model D8 advance) with monochromatic Cu-Ka radiation, 1.54178 (Å). Diffraction patterns were rearranged at room temperature within the angular range from 30 to 90º (2 Θ), with a step size of 0.02º (2 Θ) and a scan step length of 0.4 s.

Field emission scanning electron microscopy (FE-SEM).

Using a field emission SEM (JEOL JSM-6510LV) and an accelerating voltage of 20 KV, morphology and elemental composition of as-prepared nanomaterials were investigated. EMITECH K550X sputter coater was used to perform FE-SEM and gold coating processes.

Electrical studies

AC measurements were conducted within the frequency range from 500 Hz to 5 MHz. Impedance (Z), capacitance (C), resistance (R) and phase angle (υ) were instantly read with a preset automatic RCL meter (HIOK3532LCR HITESTER). Using data of Z, C, R and ϕ, at any frequency (*f*), real (έ) and imaginary (ε″) components of dielectric constant, and dielectric loss tangent (tan δ) were computed. Sample holder used for AC measurements is shown in Fig. 2.

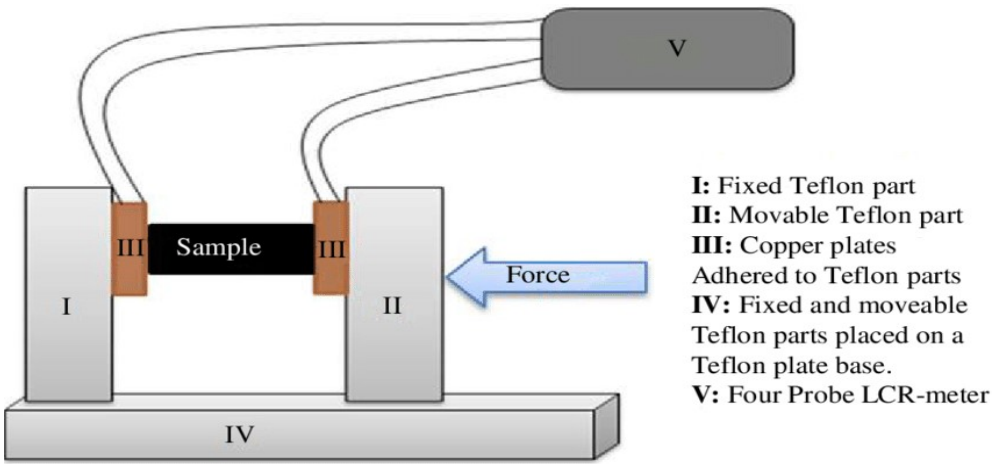

Figure 2: Sample holder was used for AC measurement.

Results and discussion

X-ray diffraction study

XRD analyses to characterize nZVI made from FC and FN are shown in Figs. 3a and 3b, respectively. The images exhibit 100% intensity for peaks at 2θ 44.87° and 44.68°, respectively, when α-Fe^0 nanoparticles are present in the sample. From Scherrer equation, it was found that FC and FN nanoparticles had average crystallographic diameters of 3.166 and 1.83 nm, respectively [12].

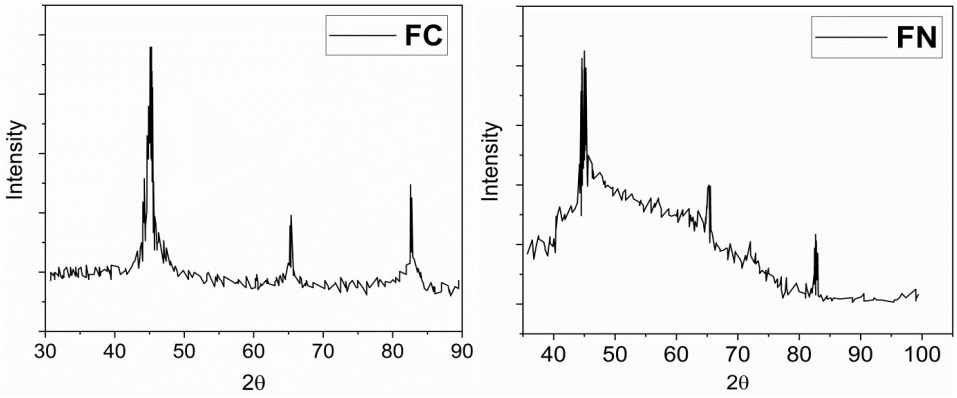

Figure 3: (a) X-ray diffraction (XRD) pattern of FC and **(b)** FN.

FE-SEM

FE-SEM, at various magnifications, was used to analyze morphology and particle size of nZVI generated from FC, as shown in Fig. 4 (a-d). Crystalline, ultrafine, spherical formations with aggregation are visible in the images.

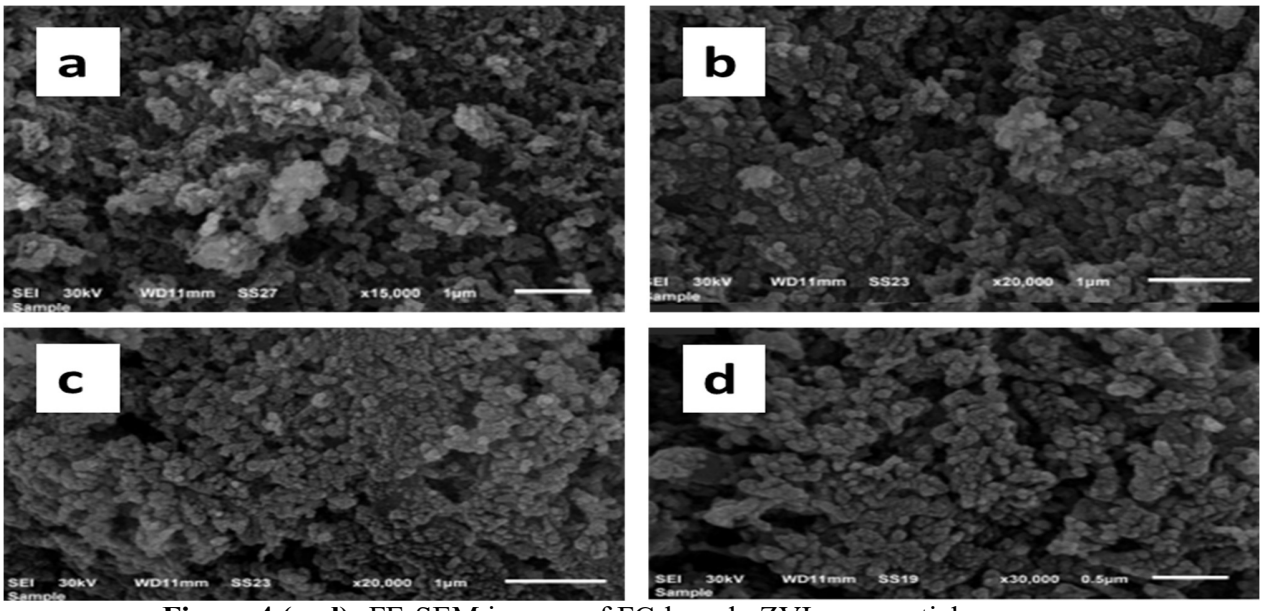

Figure 4 (a–d): FE-SEM images of FC-based nZVI nanoparticles.

It is believed that magnetic dipole-dipole interactions and the enormous surface area of individual particles are what cause iron nanoparticles to aggregate. Using SEM images, average particle size of nZVI nanoparticles (FC sample) was found to range from 50 to 100 nm. Mutually colliding tiny particles are probably due to densification, since the observed size is larger than that deduced from XRD pattern.
Morphologies of crystalline spherical networks for FN are depicted in SEM pictures (Fig. 5 e–h), with typical particle sizes ranging from 50 to 100 nm.

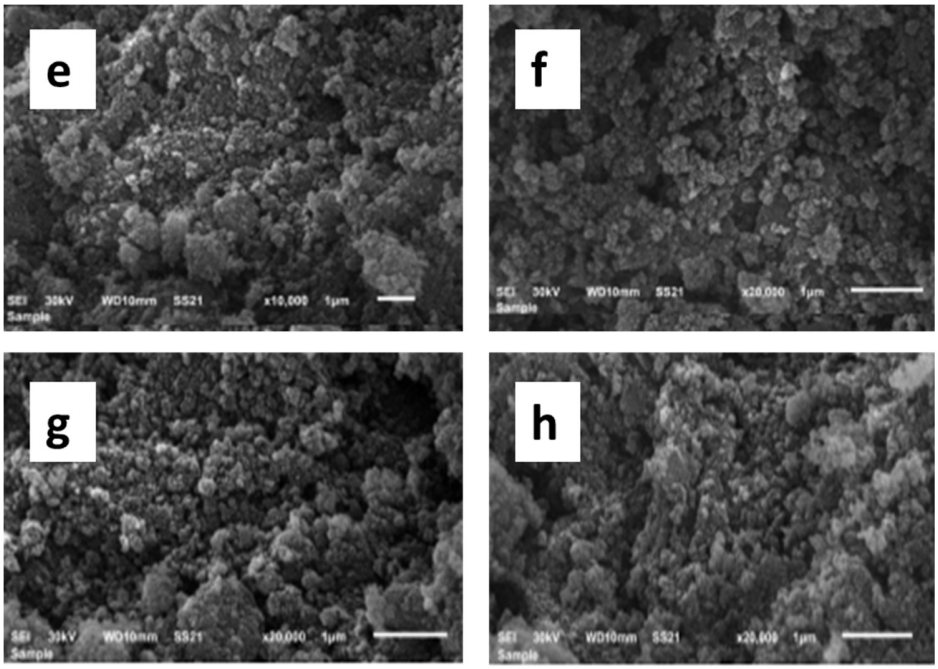

Figure 5 (e–h): FE-SEM images of the FN-based nZVI nanoparticles.

Dielectric properties

As a function of frequency, dielectric properties of the following nZVI compositions were tested and analyzed by this study: FC, FN, FC- and FN-prepared zero-valent iron with SiO_2 that calcined at 650 (FCS650 and FNS650) and 800 ºC (FCS800 and FNS800).
With the aid of dielectric analysis, two fundamental electrical characteristics of nZVI materials were established. Their two primary properties are capacitive insulating, i.e., their ability to hold electrical charge, and conduction, i.e., their capacity to transfer electrical charge.
The frequency and composition dependency of real (έ) and imaginary (ε″) parts of dielectric constant were examined and explained as a general feature of obtained results. It was concluded that real and imaginary dielectric constants from nZVI iron compositions for FC, FN, FCS650, FNS650, FCS800 and FNS800 vary with frequency (*f*), as shown in Fig. 6 a, b, and c.

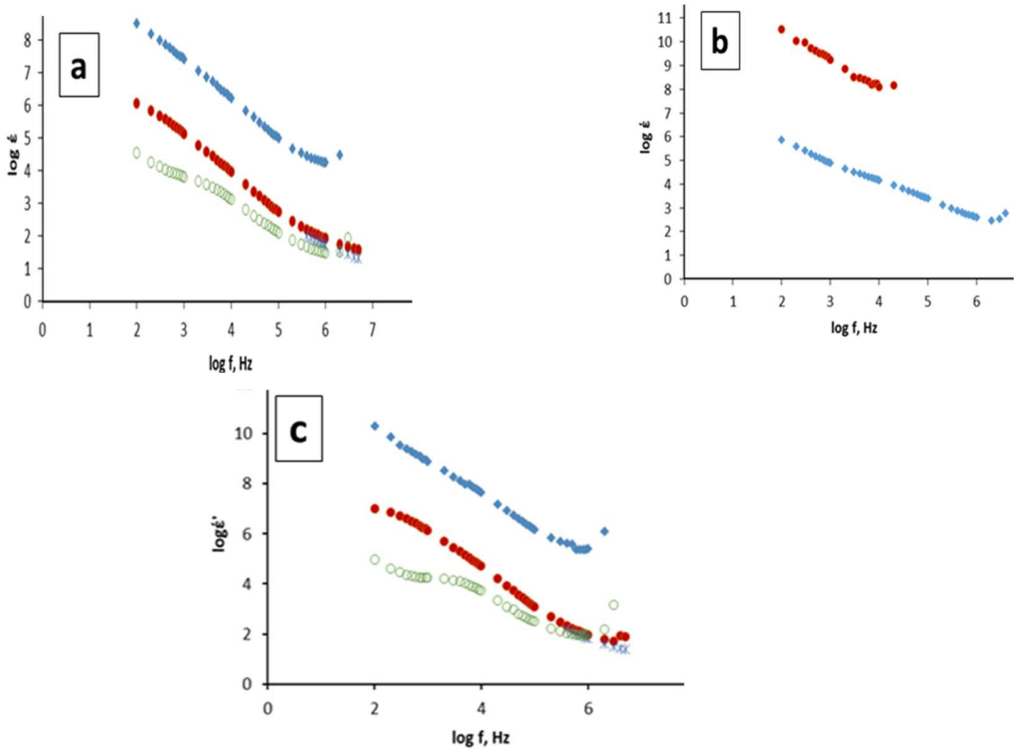

Figure 6: Real (έ) and imaginary (ε″) components of dielectric constant changes with frequencies (*f*) for **(a)** FC, FN, FCS800 and FNS800; **(b)** FCS650 and FNS650; and **(c)** FC, FN, FCS800 and FNS800.

It is evident for each composition that real (έ) and imaginary (ε″) components of dielectric constant both decrease in value as frequency rises, at room temperature. Values of $\varepsilon`$ and $\varepsilon``$ for FC and FN become frequency dependent at higher frequencies, eventually achieving a nearly constant value after reaching a maximum value at low frequencies (Table 1). Values of ε` were found to decrease with increasing frequency, due to combined effects of deformational (ionic and electronic) and relaxational (orientational and interfacial) polarization [22].

There are four sources of electronic polarization: the first is displacement of valence electrons relative to positive nucleus, which occurs at frequencies such as 1016 Hz; the second is ionic, where positive and negative ions are shifted in relation to each other; the third is dipolar, which occurs at frequencies up to 1010 Hz, when molecules in a material may change their orientation in response to an applied electric field, since they have a permanent electric dipole moment; and the fourth is space charge, which is caused by interfaces that hinder mobile charge carriers. Typical frequency range for space charge polarization is from 1 to 103 Hz. For dielectric materials, total polarization is the sum of the four polarization types above described [23, 24]. Results obtained in this investigation show that overall polarization was not significantly affected by ionic polarization. Additionally, orientational polarization decreased with

increasing frequency, because it takes longer than ionic and electronic polarization. This causes the value of ε to decrease and get closer to a constant value at higher frequencies, which are associated with interfacial polarization. Additionally, a sample's high-frequency real (έ) and imaginary (ε″) components of dielectric constant reflect its improved optical quality and reduced defects. This parameter is important for various nonlinear optical materials and their uses [25].

Table 1: Real (έ) and imaginary (ε″) components of dielectric constant for FC and FN for a selected range of frequencies (*f*).

FC			**FN**		
log *f*	**log *ε`***	**log *ε``***	**log *f***	**log *ε`***	**log *ε``***
2	8.517141	10.29946	2	6.0634	7.028084
2.30103	8.168969	9.898106	2.30103	5.837691	6.866628
2.477121	7.996137	9.559789	2.477121	5.684614	6.731304
2.60206	7.861884	9.412483	2.60206	5.566078	6.614058
2.69897	7.752451	9.286082	2.69897	5.467662	6.511132
2.778151	7.661404	9.183051	2.778151	5.38337	6.419377
2.845098	7.586409	9.100253	2.845098	5.30951	6.336554
2.90309	7.519962	9.02646	2.90309	5.245341	6.26439
2.954243	7.461461	8.962467	2.954243	5.187464	6.197963
3	7.408675	8.906876	3	5.134203	6.135486
3.30103	7.068762	8.526559	3.30103	4.783538	5.71765
3.477121	6.865173	8.294816	3.477121	4.575465	5.465311
3.60206	6.721027	8.131624	3.60206	4.435062	5.300488
3.69897	6.607467	8.002585	3.69897	4.321597	5.162792
3.778151	6.491816	7.985738	3.778151	4.225777	5.043593
3.845098	6.408754	7.880472	3.845098	4.146264	4.945795
3.90309	6.340503	7.803268	3.90309	4.077407	4.860372
3.954243	6.279319	7.733654	3.954243	4.018498	4.790034
4	6.22234	7.669767	4	3.961002	4.716288
4.30103	5.846071	7.211311	4.30103	3.587046	4.234645
4.477121	5.624173	6.942541	4.477121	3.36456	3.939705
4.60206	5.467767	6.75456	4.60206	3.21189	3.737767
4.69897	5.343517	6.608181	4.69897	3.088393	3.566371
4.778151	5.248755	6.492814	4.778151	2.994286	3.439241
4.845098	5.169851	6.39393	4.845098	2.915626	3.331743
4.90309	5.100702	6.306038	4.90309	2.84939	3.241104
4.954243	5.045411	6.244957	4.954243	2.791734	3.161801
5	4.993901	6.181048	5	2.741091	3.091871
5.30103	4.686685	5.847292	5.30103	2.440615	2.67782
5.477121	4.534939	5.706617	5.477121	2.287085	2.466494
5.60206	4.438793	5.626987	5.60206	2.187863	2.331016
5.69897	4.370959	5.587526	5.69897	2.116544	2.235103
5.778151	4.340539	5.375195	5.778151	2.061252	2.161343
5.845098	4.307531	5.377124	5.845098	2.0163	2.102435
5.90309	4.282338	5.37698	5.90309	1.979197	2.054243
5.954243	4.266863	5.383636	5.954243	1.947821	2.014583
6	4.256274	5.403648	6	1.920216	1.979585
6.30103	4.476008	6.100774	6.30103	1.757499	1.785652
-	-	-	6.477121	1.677107	1.706453
-	-	-	6.60206	1.62716	1.922624
-	-	-	6.69897	1.574856	1.898534

Table 1 and Fig. 6a illustrate frequency variation of $\varepsilon`$ and $\varepsilon``$ for FC and FN compositions. Additionally, Fig. 6a–c shows that nZVI's composition affects $\varepsilon`$ and $\varepsilon``$ values. This can be explained by the hypothesis that changing nZVI's composition will affect its iron host's structure, which will influence density of charge defect states and, eventually, dielectric characteristics [25].

A frequency dependency from dielectric loss tangent (tan (δ)) is shown in Fig. 7a, for FC and FN samples prepared with nZVI's compositions. At constant temperature, fluctuation in tan (δ) with frequency exhibits similar tendencies to those in ε", at low frequencies. This could to the fact that polarizability contribution from ionic and orientation sources diminishes up to a frequency of 10. After that, their inertia impact causes dielectric loss tangent tan (δ) to grow [26].

For different nZVI's compositions, Fig. 7 (b, c) shows frequency-dependent variation from loss tangent. The fingerprint of single relaxation peaks represents ionic conduction via nZVI's segmental motion [27]. Power of ohmic (active) component over capacitive (reactive) component is responsible for the initial rise in loss tangent at a lower frequency region. Nonetheless, the inverse pattern is observed when frequency rises and the loss tangent falls, due to the independent nature of the ohmic part and increasing reactive component with frequency. Debye theoretical approach also agrees well with resonance peak, which denotes maximum energy transfer upon application of a field [28].

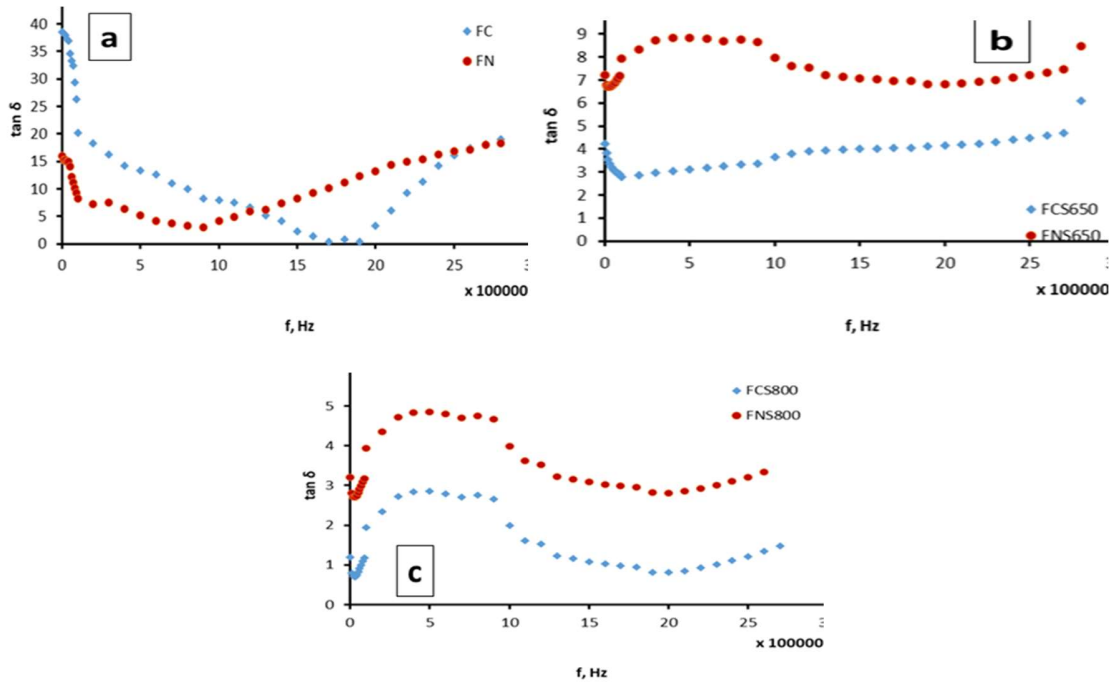

Figure 7: Variation of loss tangent (tan δ) with frequency (*f*) for (a) FC, FN, (b) FCS650, FNS650, and (c) FCS800, FNS800 for nZVI.

Electrical conductivity

Fig. 8 illustrates frequency dependence from conductivity (σ) of various nZVI's compositions, for easier visualization. According to the figure, conductivity of different compositions is low at high frequencies, and noticeably high at low ones. This behavior agrees with the well-known Debye-Falkenhagen hypothesis, which can be interpreted as the dynamic influence of the relationship between motion of the ion and ion atmosphere. Atmosphere in an electrolyte solution cannot follow center ion's movement, due to an external electric field. Ion's speed is slowed down de to this asymmetrical action. Ion atmosphere has less time to unwind and retain its asymmetry, since central ion wavers under an oscillating electric field, which causes relaxation force to decrease and conductivity to increase, at low frequencies, increasing electron mobility rate. Conductivity diminishes at high frequencies due to rapid ion oscillation, which reduces net ionic mobility in a particular direction, when there is no static or low-frequency field present [29].

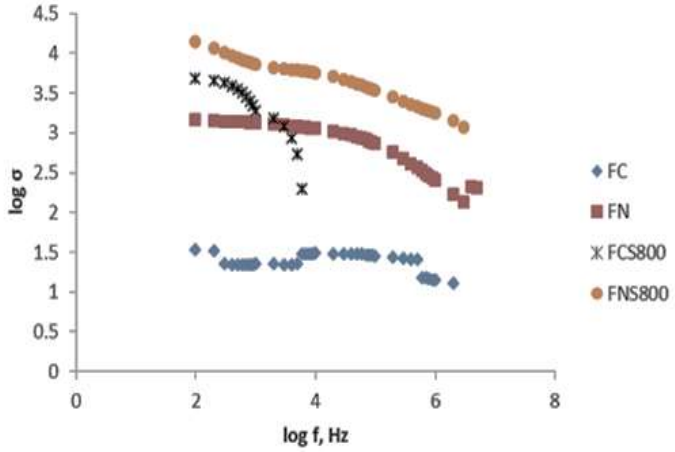

Figure 8: Variation of conductance (σ) of nZVI with frequency (*f*) for FC, FN, FCS800, and FNS800.

Conclusion

Visual observation showed that there was no oxidation during storage for weeks, after nZVI from FC and FN were effectively synthesized in a zero-oxidation state, with 100% intensity, at 2θ of 44.87 and 44.68º, with mean crystalline diameters of 3.166 and 1.83 nm, respectively. According to SEM studies, nZVI significantly tend to agglomerate in nanoscale aggregates, due to their weak surface charges. They also appear as spherical particles, and take the form of chain-like structures, with a particle size in the range from 50 to 100 nm. By using different iron salt precursors, electrical characteristics of several produced nZVI's compositions varied greatly. The choice of salt precursor thus seems to have a significant influence on distinctive physical characteristics of generated nanomaterials.

Authors' contributions

I. S. El-Hallag: performed electrical conductivities of nanoscale zero-valent iron; wrote the manuscript; elucidated the obtained results**. A. A. Al-Owais**: conceived the work; revised the manuscript. **E. H. El-Mossalamy**: prepared nanoscale zero-valent iron, and characterized its structure via SEM and XRD. All authors have read and agreed to the published version of the manuscript.

Abbreviations

C: capacitance
C_2H_6O: ethanol
FC [$FeCl_3$]: ferric chloride
FE-SEM: field emission scanning electron microscopy
FeX_n: ferric chloride or ferric nitrate
FN [$Fe(NO_3)_3$]: ferric nitrate
HNO_3: nitric acid
$NaBH_4$: sodium borohydride
NaX: sodium chloride or sodium nitrate
nZVI: nanoscale zero-valent iron
R: resistance
SEM: scanning electron microscopy
SiO_2: silica
tan δ: loss tangent
XRD: X-ray diffraction
Z: impedance

Symbols

έ: real component of dielectric constant
ε″: imaginary part of dielectric constant
f: frequency
σ: conductivity
υ: phase angle

References

1. Galdames A, Ruiz-Rubio L, Orueta M et al. Zero-Valent Iron Nanoparticles for Soil and Groundwater Remediation. Int J Environ Res Public Health. 2020;17(16):5817. https://doi.org/10.3390/ijerph17165817.
2. Pasinszki T, Krebsz M. Synthesis and Application of Zero-Valent Iron Nanoparticles in Water Treatment, Environmental Remediation, Catalysis, and their Biological Effects. Nanomater. 2020;10(5):917. https://doi.org/10.3390/nano10050917
3. Pereira GM, Cellet TSP, Rubira AF et al. Carbon-Capped Zerovalent Nickel and Cobalt Nanoparticles as Multitask Hybrid Electrocatalysts. ACS Appl Energy Mater. 2018;1(9):4939-49. https://doi.org/10.1021/acsaem.8b00955

4. Petrarca C, Poma AM, Vecchiotti G et al. Cobalt magnetic nanoparticles as theranostics: Conceivable or forgettable? Nanotechnol Rev. 2020;9(1):1522. https://doi.org/10.1515/ntrev-2020-0111
5. Barka E, Noutsopoulos C, Galani A et al. Removal of Contaminants of Emerging Concern from Wastewater Using an Integrated Column System Containing Zero Valent Iron Nanoparticles. Water. 2023;15(3):598. https://doi.org/10.3390/w15030598
6. Qiao H, Han Y, Yao L, et al. Coating zero-valent iron onto hollow carbon spheres as efficient electrocatalyst for N2 fixation and neutral Zn-N2 battery. Chem Eng J. 2023;464:142628. https://doi.org/10.1016/j.cej.2023.142628
7. Petrova E, Kotsikau D, Pankov V et al. Influence of synthesis methods on structural and magnetic characteristics of Mg–Zn-ferrite nanopowders. J Magn Magn Mater. 2019;473:85-91. https://doi.org/10.1016/j.jmmm.2018.09.128
8. Majid F, Shahin A, Ata S et al. The effect of temperature on the structural, dielectric and magnetic properties of cobalt ferrites synthesized via hydrothermal method. Z Phys Chem. 2021;235(10):1279-96. https://doi.org/10.1515/zpch-2020-1751
9. Oropeza S, Corea M, Gómez-Yáñez C et al. Zero-valent iron nanoparticles preparation. Mater Res Bull. 2012;47(6):1478. https://doi.org/10.1016/j.materresbull.2012.02.026
10. Torrey DJ, Killgore JP, Bedford NM et al. Oxidation behavior of zero-valent iron nanoparticles in mixed matrix water purification membranes. Environ Sci Water Res Technol. 2015;1:146-52. https://doi.org/10.1039/C4EW00068D
11. Yuvakkumar R, Elango V, Rajendran V et al. Preparation and characterization of zero-valent iron nanoparticles. Dig J Nanomater Biostruct. 2011;6(4):1771.
12. Alymov MI, Rubtsov NM, Seplyarskii BS et al. Preparation and characterization of iron nanoparticles protected by an oxide film. Inorg Mater. 2017;53(9):911-5. https://doi.org/10.1134/S0020168517090011
13. Yang R, Chen G, Laroche M et al. Simulation of Nanoscale Multidimensional Transient Heat Conduction Problems Using Ballistic-Diffusive Eq. and Phonon Boltzmann Eq. J Heat Transfer. 2005;127(3):298-306. https://doi.org/10.1115/1.1857941
14. Fujita K, Ando D, Uchikoshi M et al. New model for low-temperature oxidation of copper single crystal. Appl Surf Sci. 2013;276:347-58. https://doi.org/10.1016/j.apsusc.2013.03.096
15. Lenglet M, Kartouni K, Machefert J et al. Low temperature oxidation of copper: The formation of CuO. Mater Res Bull. 1995;30(4):393-403. https://doi.org/10.1016/0025-5408(95)00025-9
16. Sarathy V, Tratnyek PG, Nurmi JT et al. Aging of Iron Nanoparticles in Aqueous Solution: Effects on Structure and Reactivity. J Phys Chem C. 2008;112(7):2286-93. https://doi.org/10.1021/jp0777418

17. Greenlee LF, Torrey JD, Amaro RL et al. Kinetics of Zero Valent Iron Nanoparticle Oxidation in Oxygenated Water. Environ Sci Technol. 2012;46(23):12913-20. https://doi.org/10.1021/es303037k
18. Zhu H, Ding K, You Y et al. In-situ fabrication of exceptionally efficient traps namely nanoscale zero valent iron wrapped on mesoporous silica microspheres with different size in effectively purifying and scavenging Re(VII) and Cr(VI) from water matrices. J Environ Chem Eng. 2025;13:116367. https://doi.org/10.1016/j.jece.2025.116367
19. Namakka M, Rahman MR, Muhammad A. Insights into micro-and nano-zero valent iron materials: synthesis methods and multifaceted applications. RSC Adv. 2024;14:30411. https://doi.org/10.1039/d4ra03507k
20. Rezaei M, Khajenoori M, Nematollahi B. Synthesis of high surface area nanocrystalline MgO by pluronic P123 triblock copolymer surfactant. Pow Technol. 2011;205(1-3):112-6. https://doi.org/10.1016/j.powtec.2010.09.001
21. Jiemvarangkul P, Zhang W, Lien H-L. Enhanced transport of polyelectrolyte stabilized nanoscale zero-valent iron (nZVI) in porous media. Chem Eng J. 2011;170(2-3):482-91. https://doi.org/10.1016/j.cej.2011.02.065
22. Khan MU, Jabeen N, Nawaz S et al. Molarity Dependent Structural and Dielectric Behavior of Calcium Titanate Ceramics. Am J Eng Res. 2021;10(9):8-19. https://www. researchgate.net/publication/354462626
23. Tareev B, Tareev BM. Physics of Dielectric Materials, Mir Publ. Moscow: MIR Publ.; 1979.
24. Mott NF. Conduction in glasses containing transition metal ions. J Non-Cryst Soli. 1968;1(1):1-17. https://doi.org/10.1016/0022-3093(68)90002-1
25. Singh N, Agarwal A, Sanghi S. Dielectric relaxation, conductivity behaviour and magnetic properties of Mg substituted Ni–Li ferrites. J Alloys Comp. 2011;509(27):7543-8. https://doi.org/10.1016/j.jallcom.2011.04.126
26. Prashant KM, Sankarappa T, Vijaya KB et al. Dielectric relaxation studies in transition metal ions doped tellurite glasses. Sol Stat Sci. 2009;11(1):214-8. https://doi.org/10.1016/j.solidstatesciences.2008.05.015
27. Ranko R, Hermann W. The dielectric modulus: relaxation versus retardation. Sol Stat Ion. 1998;105(1-4):167-173. https://doi.org/10.1016/S0167-2738(97)00461-X
28. Langar A, Sdiri N, Elhouichet H et al. Conductivity and dielectric behavior of NaPO3–ZnO–V2O5 glasses. J Alloys and Compd. 2014;590:380-7. https://doi.org/10.1016/j.jallcom.2013.12.130
29. Bahgat AA. Study of dielectric relaxation in Na-doped Bi–Pb–Sr–Ca–Cu–O glasses. J Non-Cryst Sol. 1998;226(1-2):155-61. https://doi.org/10.1016/S0022-3093(97)00482-1